

# Strongly Enhanced Photovoltaic Performance and Defect Physics of Air-Stable Bismuth Oxyiodide (BiOI)

Robert L. Z. Hoye,\* Lana C. Lee, Rachel C. Kurchin, Tahmida N. Huq, Kelvin H. L. Zhang, Melany Sponseller, Lea Nienhaus, Riley E. Brandt, Joel Jean, James Alexander Polizzotti, Ahmed Kursumović, Mounji G. Bawendi, Vladimir Bulović, Vladan Stevanović, Tonio Buonassisi,\* and Judith L. MacManus-Driscoll\*

**Bismuth-based compounds have recently gained increasing attention as potentially nontoxic and defect-tolerant solar absorbers. However, many of the new materials recently investigated show limited photovoltaic performance. Herein, one such compound is explored in detail through theory and experiment: bismuth oxyiodide (BiOI). BiOI thin films are grown by chemical vapor transport and found to maintain the same tetragonal phase in ambient air for at least 197 d. The computations suggest BiOI to be tolerant to antisite and vacancy defects. All-inorganic solar cells (ITO|NiO<sub>x</sub>|BiOI|ZnO|Al) with negligible hysteresis and up to 80% external quantum efficiency under select monochromatic excitation are demonstrated. The short-circuit current densities and power conversion efficiencies under AM 1.5G illumination are nearly double those of previously reported BiOI solar cells, as well as other bismuth halide and chalcogenide photovoltaics recently explored by many groups. Through a detailed loss analysis using optical characterization, photoemission spectroscopy, and device modeling, direction for future improvements in efficiency is provided. This work demonstrates that BiOI, previously considered to be a poor photocatalyst, is promising for photovoltaics.**

Solar absorbers based on metal cations with stable  $ns^2$  valence electrons have recently come to prominence.<sup>[1]</sup> This has been fuelled by the rapid rise in the power conversion efficiency of hybrid lead-halide perovskite solar cells to over 20%.<sup>[2]</sup>

First-principles calculations suggest hybrid lead-halide perovskites to have energetically shallow intrinsic defects,<sup>[3]</sup> which may partially account for the long minority carrier lifetimes measured in these materials.<sup>[4]</sup> Recent works have suggested that the shallow defect states are linked to the formation of antibonding orbitals at band edges and increased width of the conduction and valence bands due to spin-orbit coupling.<sup>[5,6]</sup> Both factors may make it more likely that the transition levels of defect states are resonant within the bands, or positioned closer to band edges (forming shallow traps), as illustrated and detailed in ref. [5]. It has been proposed that such an electronic structure is not unique to hybrid lead-halide perovskites, but rather can occur in materials with other heavy  $ns^2$  metal cations, such as In<sup>+</sup>, Sb<sup>3+</sup>, and Bi<sup>3+</sup>.<sup>[5]</sup> Numerous papers have recently emerged exploring these compounds, particularly halides and chalcogenides based on Bi<sup>3+</sup>. These include BiI<sub>3</sub>,<sup>[7–9]</sup> (CH<sub>3</sub>NH<sub>3</sub>)<sub>3</sub>Bi<sub>2</sub>I<sub>9</sub>,<sup>[10,11]</sup> (NH<sub>4</sub>)<sub>3</sub>Bi<sub>2</sub>I<sub>9</sub>,<sup>[12]</sup> Cs<sub>3</sub>Bi<sub>2</sub>I<sub>9</sub>,<sup>[13]</sup> and CsBi<sub>3</sub>I<sub>10</sub>,<sup>[14]</sup> in addition to Cs<sub>2</sub>AgBiBr<sub>6</sub> double perovskites.<sup>[15]</sup> Calculations on some of these materials have verified the

Dr. R. L. Z. Hoye  
Cavendish Laboratory  
University of Cambridge  
JJ Thomson Ave, Cambridge CB3 0HE, UK  
E-mail: rlzh2@cam.ac.uk

Dr. R. L. Z. Hoye, L. C. Lee, T. N. Huq, Dr. K. H. L. Zhang,  
Dr. A. Kursumović, Prof. J. L. MacManus-Driscoll  
Department of Materials Science and Metallurgy  
University of Cambridge  
27 Charles Babbage Rd, Cambridge CB3 0FS, UK  
E-mail: jld35@cam.ac.uk

Dr. R. L. Z. Hoye, R. C. Kurchin, M. Sponseller, Dr. L. Nienhaus,  
Dr. R. E. Brandt, Dr. J. Jean, J. A. Polizzotti, Prof. M. G. Bawendi,  
Prof. V. Bulović, Prof. T. Buonassisi  
Massachusetts Institute of Technology  
Cambridge, MA 02139, USA  
E-mail: buonassisi@mit.edu

Prof. V. Stevanović  
Colorado School of Mines  
Golden, CO 80401, USA

Prof. V. Stevanović  
National Renewable Energy Laboratory  
Golden, CO 80401, USA

© 2017 The Authors. Published by WILEY-VCH Verlag GmbH & Co. KGaA, Weinheim. This is an open access article under the terms of the Creative Commons Attribution License, which permits use, distribution and reproduction in any medium, provided the original work is properly cited. The copyright line for this article was changed on 26 July 2017 after original online publication.

 The ORCID identification number(s) for the author(s) of this article can be found under <https://doi.org/10.1002/adma.201702176>.

DOI: 10.1002/adma.201702176

hypothesis regarding their electronic structure.<sup>[5,9,11–13]</sup> Time-correlated single photon counting (TCSPC) measurements of  $(\text{CH}_3\text{NH}_3)_2\text{Bi}_2\text{I}_9$  and  $\text{Cs}_2\text{AgBiBr}_6$ , among others, have shown that these materials exhibit lifetimes exceeding 1 ns.<sup>[11,15,16]</sup> This is significant because analysis of established thin-film solar absorbers has shown that materials with minority-carrier lifetimes of 1 ns or above have the potential to reach or exceed 10% efficiency.<sup>[17]</sup> Many of these bismuth halides and chalcogenides have also demonstrated improved air-stability compared to hybrid lead-halide perovskites.<sup>[11,13,15]</sup> However, devices based on these materials have low reported power conversion efficiencies under AM 1.5G illumination, between 0.1 and 1.2%.<sup>[11]</sup> The short-circuit current densities ( $J_{\text{SC}}$ ,  $<4 \text{ mA cm}^{-2}$ ) and external quantum efficiencies (EQEs,  $<60\%$ ) have also been poor,<sup>[1,18]</sup> in spite of efforts to extend the photoconversion range of bismuth halide semiconductors ( $J_{\text{SC}} < 3.4 \text{ mA cm}^{-2}$ , EQE  $< 25\%$ ).<sup>[14]</sup> Although higher efficiencies have been reported in bismuth- and antimony-based chalcogenides,<sup>[19–22]</sup> it is important to understand whether the broader range of  $ns^2$  compounds predicted to be defect-tolerant could also exceed 1% power conversion efficiency and reach the levels needed for commercial production after optimization.

Bismuth oxyiodide (BiOI) is another  $ns^2$  compound predicted to have antibonding orbital character at the band edges.<sup>[5]</sup> Consistent with these predictions, calculations have shown the valence band to comprise of overlapping Bi 6s, O 2p, and I 2p states, with the Bi 6s states occurring at both the bottom and top of the valence band.<sup>[23]</sup> However, the photovoltaic properties to date have been poor, with low power conversion efficiencies  $<0.1\%$  and external quantum efficiencies (EQEs)  $<5\%$  typically being reached under monochromatic excitation.<sup>[24,25]</sup> A recent report demonstrated a 1% BiOI photoelectrochemical cell under AM 1.5G illumination using an  $\text{I}_3^-/\text{I}^-$  electrolyte with an EQE of up to 60%.<sup>[18]</sup> However, aside from improving the morphology of BiOI, it was unclear whether further increases in efficiency could be achieved. Critically, BiOI has recently been found to be unstable in  $0.5 \text{ mol L}^{-1} \text{ Na}_2\text{SO}_4$  electrolyte, suggesting BiOI may be unstable in photoelectrochemical cells using liquid electrolytes.<sup>[26]</sup> But attempts to replace liquid electrolytes with solid-state hole transport layers have only resulted in 0.1% power conversion efficiency.<sup>[27]</sup>

In this work, we evaluate in detail the photovoltaic potential of BiOI through experiment and theory. We find our BiOI films to maintain the same crystallographic phase in ambient air for the duration of the 197 d testing period. These samples exhibit photoluminescence (PL) lifetimes in excess of the 1 ns threshold for promising solar absorbers. Through computations, we find BiOI to be tolerant to dominant (i.e., low formation energy) vacancy and antisite defects. We achieve EQEs of up to 80% using an all-inorganic thin film device structure: (150 nm) ITO|(8 nm)  $\text{NiO}_x$ |(440–940 nm) BiOI|(25 nm) ZnO|(100 nm) Al. Our devices exhibit negligible hysteresis, and the  $J_{\text{SC}}$  values and power conversion efficiencies are nearly double those of previous reports of not only BiOI but also other bismuth halide and chalcogenide photovoltaics explored as part of the recent effort by many groups to investigate  $ns^2$  compounds. To provide direction for future research to build upon our work, we analyze the losses in our devices through optical analysis, photoemission spectroscopy, device modeling, and photothermal deflection spectroscopy.

We grew BiOI thin films by chemical vapor transport (CVT) inside a two-zone horizontal tube furnace, using  $\text{BiI}_3$  as the source powder and an  $\text{Ar}/\text{O}_2$  gas mixture to oxidize the vaporized  $\text{BiI}_3$ . This process is similar to vapor transport deposition systems used industrially.<sup>[28]</sup> 2D diffraction patterns showed the films to be polycrystalline and isotropic (Figure 1a),<sup>[29]</sup> and 1D line scans (Figure 1b) showed that all peaks matched those of tetragonal BiOI ( $P4/nmm$ , space group 129).<sup>[23,30]</sup> No additional peaks were observed, apart from amorphous broadening from the glass substrate between  $20^\circ$  and  $28^\circ$ , indicating our material was phase-pure down to the detection limits of our diffractometer. We stored our BiOI thin film in ambient air under standard laboratory illumination and repeatedly measured the 1D diffraction pattern over a 197 d period. During this time, the temperature varied between 20 and  $25^\circ\text{C}$ , and the relative humidity between 45 and 67%. We found both the diffraction peak positions and film appearance to remain unchanged over time (Figure 1b), indicating that BiOI maintained the same phase under the tested conditions. This is a two orders of magnitude improvement in stability over methylammonium lead iodide.<sup>[11]</sup>

We measured the bandgap of BiOI to be 1.93 eV: The indirect bandgap<sup>[31]</sup> was taken into account by using an exponent of 0.5 in the vertical axis term on the Tauc plot (Figure 1c, inset). This agreed with the photoluminescence peak centered at 1.9 eV (Figure 1c), red appearance of the films (Figure 1b), and previous reports.<sup>[32,33]</sup> Our semilogarithmic plot of the absorption coefficient against photon energy<sup>[29]</sup> also yielded a bandgap of 1.93 eV (Figure S1, Supporting Information). A bandgap of 1.9 eV is highly suitable for a top-cell absorber with silicon in tandem photovoltaics.<sup>[34]</sup> The absorption coefficients are on the order of  $10^4 \text{ cm}^{-1}$  (Figure 1c), which are on par with other indirect-bandgap solar absorbers.<sup>[1]</sup>

To evaluate the transport properties of our CVT BiOI films, we measured their lifetimes by TCSPC. The PL decays were fluence-independent and exhibited initial bowing, followed by a tail with a slower decay. We fitted the PL decay with a simple biexponential model, as well as with a model<sup>[16]</sup> accounting for generation, surface and bulk recombination, and diffusion within the film (Section S2, Supporting Information). These models were convolved with the instrument response function and fitted to the measured PL decay. In both cases, the bulk lifetime was  $>1 \text{ ns}$ . The fitted recombination model yielded a bulk lifetime of 2.7 ns (Table S2, Supporting Information), indicating BiOI to be worth investigating for photovoltaic applications.

To understand the tolerance of BiOI to intrinsic point defects, we calculated the formation energy as a function of Fermi energy of vacancy ( $V_{\text{Bi}}$ ,  $V_{\text{O}}$ , and  $V_{\text{I}}$ ) and antisite defects ( $\text{O}_{\text{I}}$ ,  $\text{I}_{\text{O}}$ ,  $\text{Bi}_{\text{O}}$ ,  $\text{Bi}_{\text{I}}$ ,  $\text{O}_{\text{Bi}}$ ,  $\text{I}_{\text{Bi}}$ ). These calculations were performed using an automated supercell approach with finite size corrections applied, as detailed elsewhere.<sup>[35–37]</sup> A prerequisite to performing these calculations is to assess the stability of BiOI elements because the formation of defects involves the addition or removal of atoms. The assessment was performed by using the fitted elemental-phase reference energies (FERE) approach for calculating the enthalpies of formation and a standard set of equations to determine the stability.<sup>[38]</sup> A map of the thermodynamically stable phases under different chemical potentials for Bi, I, and O is shown in Figure 2a, with the phase-stable region for BiOI indicated. The defect formation

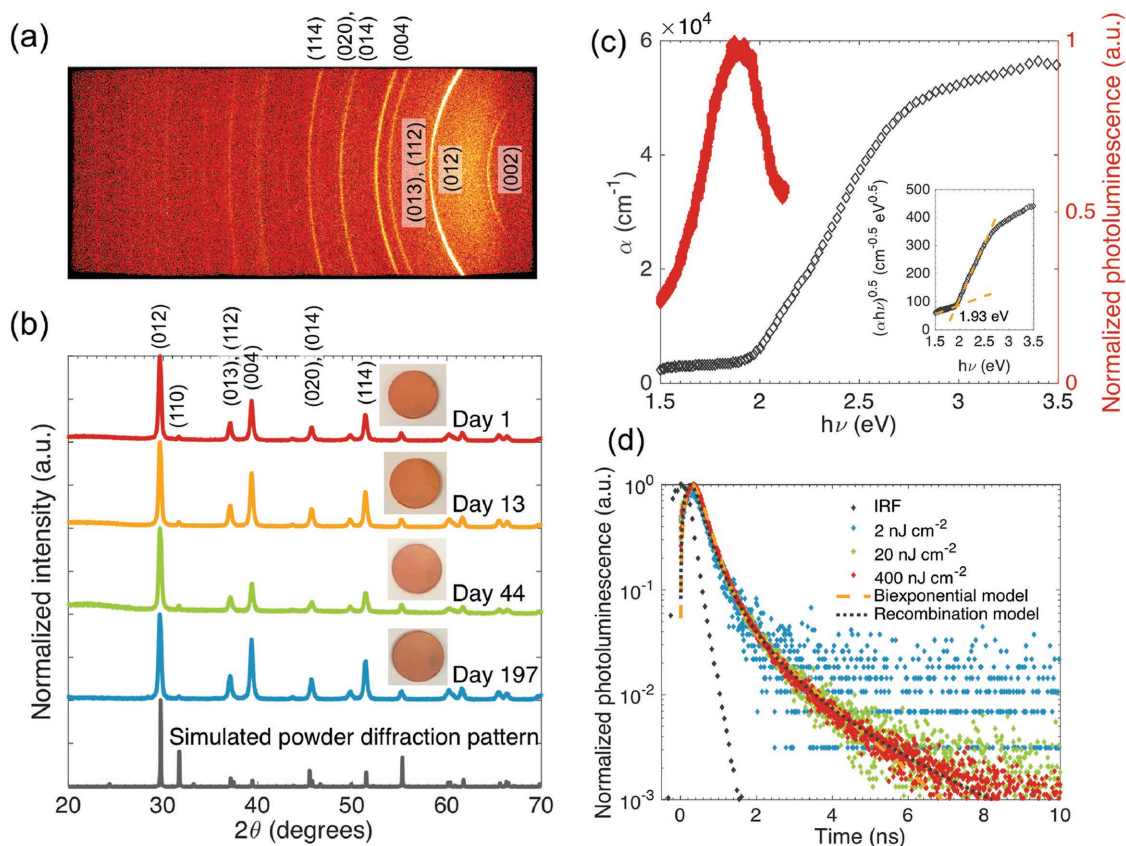


**Figure 1.** Characterization of BiOI thin films. a) 2D X-ray diffraction pattern, b) 1D X-ray diffraction patterns in ambient air over time, and c) absorption and spectrally resolved photoluminescence measurements. d) Time-correlated single photon counting measurements of BiOI in air. Biexponential and recombination models were fit to the trace measured under  $400 \text{ nJ cm}^{-2}$  (detailed in Section S2, Supporting Information).

energies were calculated at the four extrema of this phase-stable region (Figure 2b). The slopes in the diagrams indicate the defect charge state. Positively sloped defects (e.g.,  $V_{\text{O}}$ ) behave as donors, while negatively sloped defects (e.g.,  $V_{\text{Bi}}$ ) behave as acceptors. The lowest-energy cross-over between the donor and acceptor defects is, to a first approximation, the position where the intrinsic equilibrium Fermi energy is pinned, as mandated by the charge-neutrality condition. These points (between  $V_{\text{Bi}}$  and  $V_{\text{I}}$  for points A and B; between  $O_{\text{I}}$  and  $V_{\text{I}}$  for points C and D) are indicated by black arrows in Figure 2b. Calculations show that for all considered chemical potentials the equilibrium Fermi energy is located near the middle of the bandgap, indicating the intrinsic nature of BiOI.

We used X-ray photoemission spectroscopy (XPS) to check our predictions of Fermi energy position. Using a method reported by Kraut et al.,<sup>[29,39,40]</sup> we convolved our calculated density of states for BiOI with a Gaussian representing instrument broadening. This convolved model was fit to the leading edge of our measured XPS spectrum (Figure 2c). We measured the valence band position relative to the Fermi level ( $VB-E_{\text{F}}$ ) to be 1.01 eV, slightly larger than half the bandgap of 1.9 eV. This shows the Fermi level to be close to mid-gap, in agreement with our calculations discussed above.

The energy levels of defect states can be determined from the calculated defect charge transition levels. For a particular

defect, the charge transition levels are located at the Fermi energies at which there is a change in the charge state of the defect. Charge transition levels that occur away from the band edges behave as deep traps and are detrimental to PV performance. Points A and B represent films grown under I-rich conditions. The prevalent defects are those with the lowest formation energies at the equilibrium Fermi energy ( $V_{\text{Bi}}$ ,  $O_{\text{I}}$ , and  $V_{\text{I}}$ ). These are all shallow because their charge transition levels are either inside or close to the band edges. Other defects have significantly higher formation energies ( $\Delta H_{\text{D,q}} > 1 \text{ eV}$ ), implying that they have much lower equilibrium concentrations (Figure 2b) and can likely be neglected. In addition, we calculated a high dielectric constant (electronic + ionic) of 45, which can help to further screen charged defects, contributing to a low trapping probability. Our defect calculations therefore suggest BiOI would behave as a defect-tolerant material.

Points C and D represent films grown under Bi-rich conditions. At these points, the calculated formation energies at the donor–acceptor cross-over point are close to 0 eV, which indicates high intrinsic concentrations of corresponding defects. As the deviations of the formation energies from the zero value are within the accuracy of our stability calculations, quantitative predictions of the defect concentrations at points C and D require more accurate evaluation of the materials stability and the corresponding ranges of the chemical potentials.

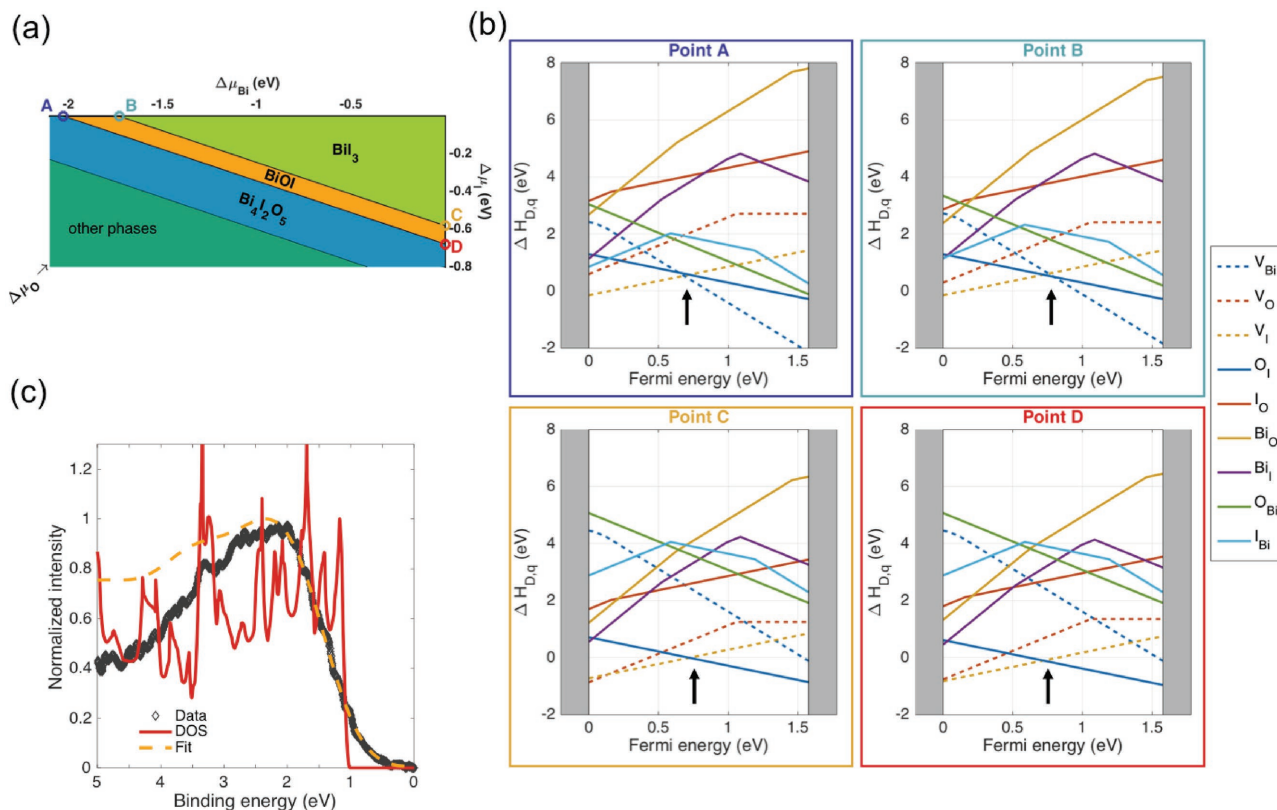


**Figure 2.** Computations on BiOI. a) Phase diagram of the Bi–O–I system, focusing on phases around BiOI, with the equilibrium region for BiOI shown. b) Formation energy of intrinsic point defects in BiOI at the four extrema in the phase-stable region for BiOI. Points A and B correspond to I-rich growth conditions, whereas points C and D correspond to Bi-rich conditions. c) X-ray photoemission spectroscopy of the valence spectrum of BiOI on FTO-coated glass, fit with the density of states of BiOI convolved with a Gaussian with a FWHM of 0.48 eV to account for instrument broadening.

Nevertheless, Figure 2b shows that the lowest formation-energy (most abundant) defects,  $V_I$  and  $O_I$ , are also shallow.

To investigate the photovoltaic potential of BiOI, we developed an all-inorganic device structure, comprised of  $\text{NiO}_x$  hole transport layer and ZnO electron transport layer (Figure 3a). An important challenge was that our BiOI has a textured surface morphology (Figure 3b), with the grains preferentially oriented along the {012} planes (Figure S3, Supporting Information). To ensure a continuous electron transport layer, we deposited ZnO by atmospheric pressure chemical vapor deposition (AP-CVD).<sup>[41]</sup> Figure 3a–c shows that ZnO was conformal to BiOI.

Using this device structure, we were able to achieve EQEs up to 80% (Figure 3d). The integrated  $J_{SC}$  values of the EQE spectra closely matched the  $J_{SC}$  values measured through current density–voltage ( $J$ – $V$ ) sweeps (Table 1). An EQE of 80% exceeds the highest previously reported for BiOI<sup>[18]</sup> and is higher than recently reported EQEs from other bismuth halides and chalcogenides (discussed in the Introduction).<sup>[10,14,42]</sup>

We found that we could further improve efficiency by lowering the deposition temperature of ZnO from 100 to 80 °C. This led to a reduction in the dark current densities (Figure 4a) and an increase in the reverse-sweep fill factors from  $32 \pm 2$  to  $39 \pm 3\%$ . Conversely, increasing the deposition temperature to 120 °C led to increases in dark current density and a sub-optimal fill factor of  $33 \pm 4\%$ . Lowering the ZnO deposition temperature therefore allowed us to achieve an increase in

the power conversion efficiency to 1.8% with negligible hysteresis, as can be seen from the  $J$ – $V$  sweeps (Figure 4c) and reverse and forward efficiency values (Table 2). The EQE of our highest-performing device (Figure 4d) had an integrated  $J_{SC}$  of  $7.3 \text{ mA cm}^{-2}$ , which was again comparable to the measured reverse and forward sweep  $J_{SC}$  values (Table 2). These  $J_{SC}$  values are almost double the highest previously reported for BiOI.<sup>[18]</sup> An important reason for the high performance of our devices is the densely packed morphology of the  $\text{NiO}_x$  (Figure S12, Supporting Information) and BiOI layers (Figure 3a,b), as well as our conformal AP-CVD ZnO layer (Figure 3a–c). These led to low leakage, as can be seen from the low reverse-bias dark current density of our optimized device (Figure 4a). Notably, our all-inorganic device structure outperformed our devices based on  $\text{TiO}_2$  and spiro-OMeTAD (Figure S13, Supporting Information). Our inorganic BiOI device was also more stable under constant illumination in air than a similarly structured  $\text{CH}_3\text{NH}_3\text{PbI}_3$  device (ITO| $\text{NiO}_x$ | $\text{CH}_3\text{NH}_3\text{PbI}_3$ | $\text{PC}_{60}\text{BM}$ |Al), as illustrated in Figure 3e. We found BiOI devices to maintain their performance when stored in ambient air (21 °C, 60% relative humidity) for 3 d, whereas  $\text{CH}_3\text{NH}_3\text{PbI}_3$  devices degraded from 14.8% on day 1 to 0.07% on day 3, with obvious corrosion of the Al top electrode (Figure S14, Supporting Information).

To provide direction for future developments, we further analyzed losses in our BiOI devices. We measured the reflectance

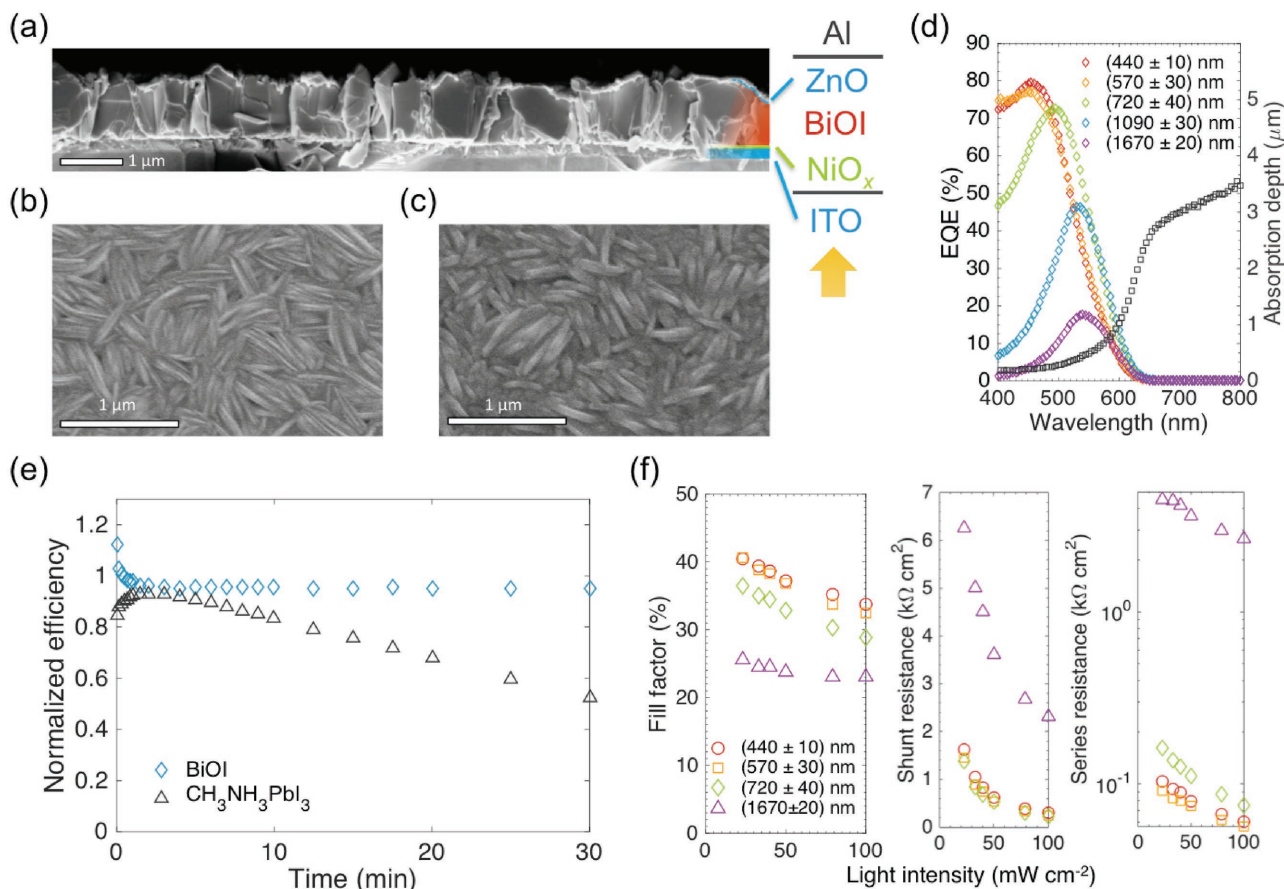


**Figure 3.** Characterization of ITO|NiO<sub>x</sub>|BiOI|ZnO|Al devices. a) Cross-sectional SEM image of the device stack without Al. Top-down SEM images of b) BiOI and c) ZnO on BiOI. d) External quantum efficiency (EQE) measurements of BiOI devices with different thicknesses. The absorption depth is the inverse of the absorption coefficient, corresponding to the thickness where the transmitted light is  $e^{-1}$  of the incident light. e) Performance of BiOI and CH<sub>3</sub>NH<sub>3</sub>PbI<sub>3</sub> devices over time under constant 1 sun illumination. The normalized efficiencies shown were obtained from measuring the maximum power over time at 0.4 V for BiOI and 0.74 V for CH<sub>3</sub>NH<sub>3</sub>PbI<sub>3</sub>, and normalized to the efficiencies measured from  $J-V$  curves. f) Intensity-dependent measurements of BiOI devices. The dependence of  $J_{SC}$ ,  $V_{OC}$ , and power conversion efficiency with illumination intensity are shown in Section S4 (Supporting Information). The thicknesses shown were measured by cross-sectional SEM, detailed in Section S3 (Supporting Information).

of our full device stack using UV–visible spectrophotometry with an integrating sphere. The reflectance from the front surface of our device led to an EQE loss of between 3 and 13% over the spectral range, with a total loss in  $J_{SC}$  of 1.7 mA cm<sup>-2</sup> (Figure 4e). The remaining optical losses were approximated using Beer–Lambert law and detailed in Section S5 (Supporting

**Table 1.** Comparison of peak EQE, integrated  $J_{SC}$  and  $J_{SC}$  measured under 1 sun AM 1.5G illumination (corrected for spectral mismatch) for the same devices. Average  $J_{SC}$  from  $J-V$  curves of five devices for each thickness are also shown.

BiOI thickness [nm]	Peak EQE [%]	Integrated $J_{SC}$ [mA cm <sup>-2</sup> ]	Measured $J_{SC}$ [mA cm <sup>-2</sup> ]	Average $J_{SC}$ [mA cm <sup>-2</sup> ]
440 ± 10	79.5	6.4	6.2	5.5 ± 0.5
570 ± 30	80.2	6.4	5.8	5.6 ± 0.4
720 ± 40	72.6	6.5	6.6	6.3 ± 0.5
1090 ± 30	46.4	3.5	3.9	4.0 ± 0.1
1670 ± 20	17.6	1.3	0.6	0.4 ± 0.1

Information). These regions are shaded in gray in Figure 4e and boundaries tentatively indicated with dashed lines. We note that accurately determining each of these losses requires complex and detailed optical modeling that accounts for reflection from the textured top Al electrode, which is beyond the scope of this work. Nevertheless, our current optical analysis suggests that an important loss mechanism in our devices is due to photogenerated carriers not being collected.

To gain further insight into the dynamics of photogenerated charge carriers, we performed intensity-dependent device measurements. The fill factors decreased with increasing light intensity (Figure 3f), which led to a decrease in power conversion efficiency, despite the increase in both current density and open-circuit voltage (Figure S15, Supporting Information). This can be explained by the observed decrease in shunt resistance at elevated light intensities (Figure 3f), which is consistent with an increase in photogenerated carrier recombination when carrier densities rise. The series resistance also decreased with increasing light intensity, consistent with increased carrier concentration due to photogenerated carriers leading to increased

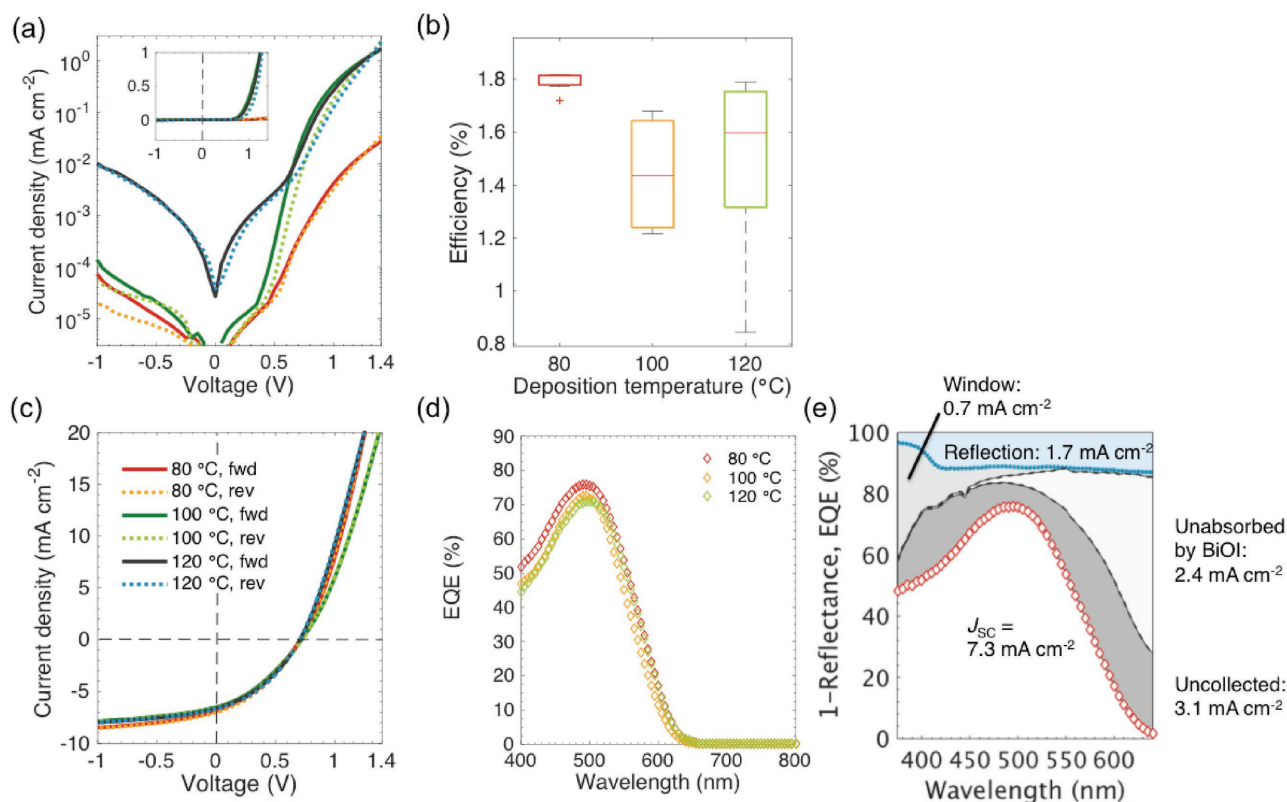


**Figure 4.** Investigating the influence of ZnO deposition temperature on the performance of BiOI devices. a) Forward- and reverse-sweep dark  $J$ - $V$  curves, b) boxplot of efficiencies, c) forward- and reverse-sweep light  $J$ - $V$  curves, and d) EQE spectra. The thicknesses of the BiOI layers used in this comparison were between 720 and 940 nm (Section S3, Supporting Information). The legends for parts (a) and (c) are the same. e) Above-bandgap optical loss analysis for 1.8% BiOI device ( $920 \pm 40$  nm BiOI thickness, Figure S10, Supporting Information).

conductivity in the BiOI layer. We also measured the effect of BiOI thickness on EQE and found the peak EQE to decrease with increasing thickness above  $570 \pm 30$  nm and shift to longer wavelengths (Figure 3d).

We hypothesized that these observations were due to a mechanism opposing carrier collection in our devices. If the density of photogenerated carriers were high, then there would be increased recombination due to limited carrier extraction, resulting in the shunt resistance decreasing with increasing illumination. In thicker BiOI layers, carriers (particularly electrons generated close to the  $\text{NiO}_x/\text{BiOI}$  interface by short-wavelength photons) need to migrate longer before they are collected, resulting in lower peak and short-wavelength EQEs. Processes reducing carrier collection would exacerbate these trends. But if this mechanism were dominant, we would expect the series resistance to remain constant with thickness, which is not the case (Figure 3f).

**Table 2.** Average performance of seven BiOI devices with ZnO deposited at 80 °C. Format: average  $\pm$  uncertainty (best value).

	$J_{sc}$ [mA cm <sup>-2</sup> ]	$V_{oc}$ [V]	FF [%]	PCE [%]
Rev	$6.3 \pm 0.5$ (7.0)	$0.75 \pm 0.01$ (0.75)	$39 \pm 3$ (43)	$1.79 \pm 0.03$ (1.82)
Fwd	$6.3 \pm 0.4$ (6.9)	$0.75 \pm 0.01$ (0.75)	$37 \pm 3$ (42)	$1.74 \pm 0.03$ (1.81)

An alternative hypothesis is that BiOI forms a depleted heterojunction with ZnO: When BiOI is thicker, the intensity of light reaching the depleted heterojunction is lower, leading to lower EQEs. Our models describing this hypothesis are detailed in Section S6 (Supporting Information). These models fit the data well and we obtained a depletion width of 570 nm from our analysis of devices with  $570 \pm 30$  nm or thicker BiOI.

To improve our understanding of the operation of our devices and loss mechanisms, we measured the band structure of our device stack through photoemission spectroscopy (PES) on each layer. The XPS measurements of  $\text{NiO}_x$  and all of the ultraviolet photoemission spectroscopy (UPS) measurements were fit with tangents to the edge and background on linear scales (Figure 5a,f). The  $V_B-E_F$  from XPS of BiOI was fit using the method described above for Figure 2c. We checked to ensure that there was no beam damage and negligible charging during these measurements (Section S7, Supporting Information).<sup>[29]</sup>

We found the  $V_B-E_F$  of BiOI to decrease with increasing thickness from 1.3 to 0.9 eV over the thickness range studied (Figure 5 and Table 3). The work function of BiOI also increased from 4.6 to 5.1 eV over the same thickness range (Table 3). We interpreted this as BiOI exhibiting band bending. The BiOI thin film (without top contacts) farthest away from the  $\text{NiO}_x/\text{BiOI}$  junction (i.e., thickest BiOI) would then have band positions closest to equilibrium conditions. The 720 nm thick BiOI had a Fermi level 0.9 eV from the valence band, which is close to

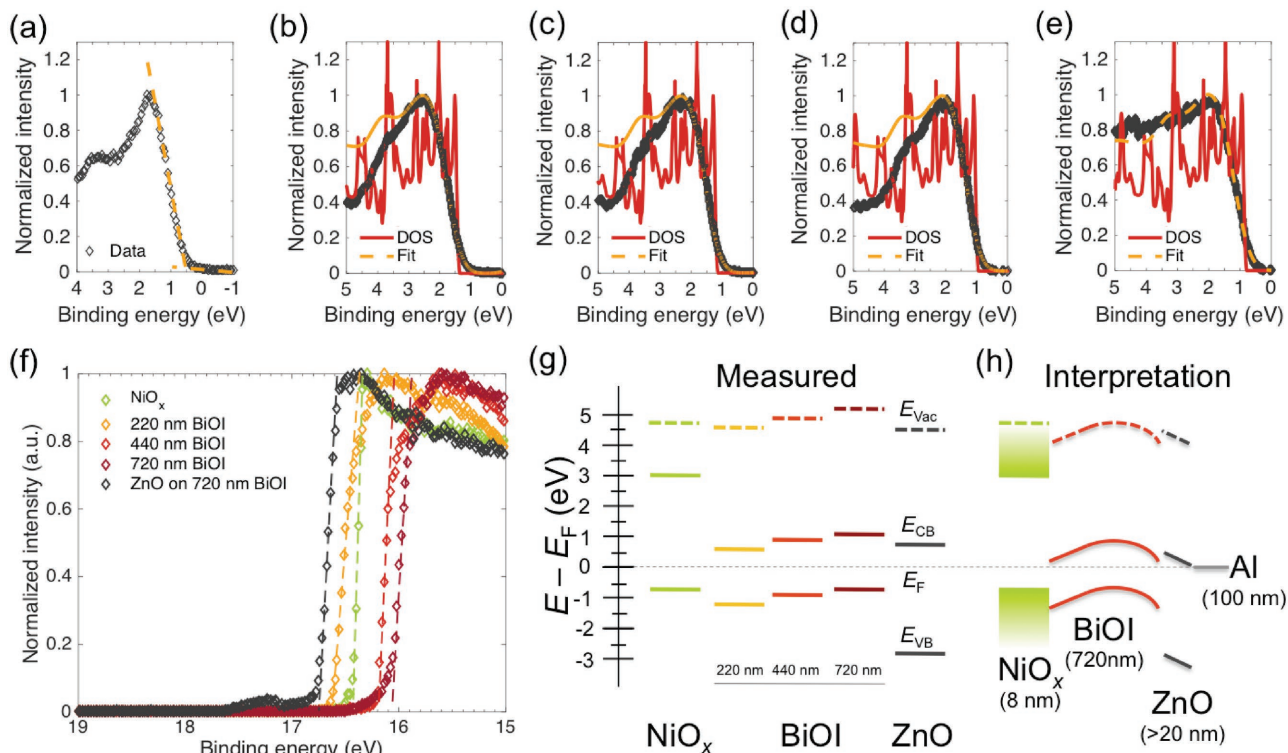


**Figure 5.** Photoemission spectroscopy measurements of BiOI to determine band structure. a–e) X-ray photoemission spectroscopy (XPS) measurements of NiO<sub>x</sub> on ITO (a), 220 nm BiOI (b), 440 nm BiOI (c), 720 nm BiOI on NiO<sub>x</sub> (d), and ZnO on 720 nm BiOI deposited on NiO<sub>x</sub>/ITO (e). It is noted that the thickness measurements were performed on a different set of films but grown under the same conditions (Section S3, Supporting Information). f) Ultraviolet photoemission spectroscopy measurements on the same set of films used for XPS measurements. g) Measured alignment of device stack. h) Interpreted band alignment based on expected effect of Al top electrode.

that measured for BiOI on FTO (Figure 2c). The work function was 5.1 eV from vacuum level, which is larger than that of NiO<sub>x</sub> (4.8 eV, Table 3). BiOI in contact with NiO<sub>x</sub> would then exhibit downward band bending at the interface. This band bending interpretation is also consistent with our work function measurements, with the vacuum level varying with BiOI thickness as illustrated in Figure 5g. Additionally, band bending in BiOI occurring over hundreds of nanometers is consistent with a low carrier concentration that would occur in materials with a mid-gap Fermi level. An alternative explanation for our PES results is that BiOI has fewer pinholes as it becomes thicker. However, top-down scanning electron microscopy (SEM) images did not

**Table 3.** Valence band position relative to the Fermi level (VB- $E_F$ ) from XPS measurements, and work function (WF) fit from UPS measurements (uncertainties in Section S7, Supporting Information). VB and conduction band (CB) positions are relative to vacuum level.

Layer	VB- $E_F$ [eV]	WF [eV]	VB [eV]	$E_g$ [eV]	CB [eV]
NiO <sub>x</sub> on ITO	0.6	4.8	5.4	3.6 <sup>[43]</sup>	1.8 <sup>[43]</sup>
220 nm BiOI on NiO <sub>x</sub> /ITO	1.3	4.6	5.9	1.9	4.0
440 nm BiOI on NiO <sub>x</sub> /ITO	1.1	5.0	6.1	1.9	4.2
720 nm BiOI on NiO <sub>x</sub> /ITO	0.9	5.1	6.0	1.9	4.1
ZnO on BiOI/NiO <sub>x</sub> /ITO	2.8 <sup>a)</sup>	4.5	7.3	3.5	3.8

<sup>a)</sup>From UPS measurements.

reveal any detectable pinholes in any of the samples measured by PES (Figure S36–S40, Supporting Information).

We note that the valence and conduction band positions of BiOI (6.0 and 4.1 eV relative to vacuum level, respectively) are close to those we measured from 2  $\mu\text{m}$  thick BiOI on TiO<sub>2</sub> (6.4 and 4.4 eV, Figure S41, Supporting Information). Our measurements of the valence band position of our films are close to literature reports (2.0–2.1 eV relative to H<sup>+</sup>/H<sub>2</sub>,<sup>[26,32]</sup> or 6.4–6.5 eV relative to vacuum).<sup>[44]</sup>

We also characterized the BiOI/ZnO interface. The ZnO was deposited in the same way for the PES measurements as for our devices. XPS measurements of ZnO on BiOI revealed an onset at 0.8 eV (Figure 5e). We attribute this to the VB- $E_F$  of the underlying BiOI layer, particularly because we observed Bi and I core levels in our XPS measurements (Figure S25, Supporting Information). The onset of 0.8 eV is close to that measured for 720 nm BiOI, indicating that the top ZnO layer does not locally n-dope the BiOI. UPS measurements revealed a leading-edge onset at 2.8 eV, which is likely the VB- $E_F$  of the ZnO overlayer (Figure S34, Supporting Information). This is because our UPS measurements are more surface-sensitive than XPS measurements and because the UPS spectra of ZnO on BiOI more closely resemble the shape of the UPS measurements of ZnO grown on different substrates (Figure S35, Supporting Information) than those of BiOI (Figure S31–S33, Supporting Information). There were also two features at high binding energy in the UPS spectrum of ZnO on BiOI (Figure 5f).

The dominant onset likely corresponds to the secondary-electron cutoff for ZnO, giving a work function of 4.5 eV. Our ZnO (3.5 eV bandgap, Figure S42, Supporting Information) therefore has valence and conduction band extrema located at 7.3 and 3.8 eV relative to the vacuum level. While we may expect there to be a 0.3 eV electron extraction barrier at the BiOI|ZnO interface, our low-temperature grown ZnO has sub-bandgap states (Figure S42, Supporting Information) that may accept electrons injected from BiOI.<sup>[45]</sup> The BiOI|ZnO interface could therefore allow barrier-less electron transport, in agreement with the absence of any kink at the  $V_{OC}$  point of our  $J$ - $V$  curves (Figure 4c).

Therefore, from our PES measurements, we observed band bending of BiOI next to  $NiO_x$ . This downward band bending at the  $NiO_x$ |BiOI interface would lead to electron drift to  $NiO_x$  and hole drift to ZnO, respectively, where they would be blocked by the low electron affinity of  $NiO_x$  and high ionization potential of ZnO. The observed band bending in BiOI would then oppose carrier collection and supports our first hypothesis. We would then expect that we could overcome this loss mechanism by increasing the work function of the hole transport layer to exceed that of BiOI (5.1 eV), leading to upward bending of BiOI at the interface with  $NiO_x$  that could aid charge separation. This could improve the fill factor and short-circuit current density, as well as open-circuit voltage ( $V_{OC}$ ). We did not observe a depleted heterojunction between BiOI and ZnO, in opposition to our second hypothesis. This may be because the ZnO we deposited at 80 °C had a low carrier concentration, with a Fermi level measured to be 0.7 eV ( $27kT$ ) below the conduction band minimum. The donor density would then be insufficient to lead to band bending in BiOI. However, the Al top electrode can donate a high density of electrons and cause depletion of the neighboring BiOI and thin ZnO layer, as illustrated in Figure 5h. This scenario seems plausible since our simulations suggest it is unlikely that charge separation is driven only by diffusion (Section S6, Supporting Information). If our second hypothesis were correct, we would expect to improve device performance by illuminating through the ZnO layer.

We identified another possible way of improving device performance by investigating the composition of the BiOI|ZnO interface. Analysis of the XPS core spectra showed us that BiOI was I-deficient after depositing ZnO in air (Table 4), despite minimizing the ZnO growth temperature to minimize damage to BiOI (Figure 4). Controlling the surface chemical state, for example, with a vacuum-deposited protective layer, may allow us to avoid changing the surface composition of BiOI.

Finally, we note that the  $V_{OC}$  of our devices ( $0.75 \pm 0.01$  V, Table 2) is below the Shockley–Queisser limit for a 1.9 eV bandgap material (1.6 V).<sup>[46]</sup> One factor possibly limiting the  $V_{OC}$  is nonradiative recombination due to shunt pathways or limited carrier collection (as discussed above). From the  $J$ - $V$  curves of our devices, we estimated the shunt resistance to be

$230 \Omega \text{ cm}^2$  under 1 sun illumination (Figure 3f). Previous analysis of Au|Cu<sub>2</sub>O|Ga<sub>2</sub>O<sub>3</sub> devices has indicated that a shunt resistance of  $230 \Omega \text{ cm}^2$  would result in the  $V_{OC}$  being 0.8 V below the Shockley–Queisser limit, which is similar to the magnitude of  $V_{OC}$  loss we observed for our BiOI devices.<sup>[47]</sup> Another factor limiting the  $V_{OC}$  could be the offset between the work function of the  $NiO_x$  hole transport layer (4.8 eV, Table 3) and electron injection level at either the BiOI conduction band minimum (4.1 eV, Table 3) or Al top electrode ( $4.25 \pm 0.05$  eV).<sup>[48,49]</sup> These offsets (0.7 and 0.55 eV, respectively) could limit the splitting in quasi-Fermi levels for electrons and holes and thereby limit  $V_{OC}$ . Interfacial recombination could also limit  $V_{OC}$ . As discussed above, BiOI is I-deficient at the interface with ZnO, which may be a source of recombination. Disorder in the BiOI absorber could lead to  $V_{OC}$  losses, for example due to potential fluctuations in the bandgap.<sup>[50]</sup> Using photothermal deflection spectroscopy, we measured the Urbach energy to be 70 meV for BiOI grown on quartz, and 90 meV for BiOI grown on  $NiO_x$  on quartz (Figure S43, Supporting Information). Cu<sub>2</sub>ZnSnS<sub>4</sub> has a similar Urbach energy and has a  $V_{OC}$  0.5 V below its Shockley–Queisser limit value.<sup>[46,50]</sup> Band tails and sub-bandgap states present in the  $NiO_x$  (Figure S43, Supporting Information) and ZnO layers (measured previously,<sup>[45,51]</sup> and from Figure S42, Supporting Information) can also lead to  $V_{OC}$  losses due to carrier thermalization or recombination from the band tails.<sup>[45,52]</sup> Further device modeling and temperature-dependent  $V_{OC}$  measurements are required to quantify the magnitudes of these different effects. However, we would expect that engineering the energy levels and interfaces with charge transport layers discussed above would also lead to improvements in  $V_{OC}$ .

In conclusion, we have demonstrated photovoltaic devices with BiOI grown by industrially compatible chemical vapor transport. The thin films of BiOI were shown to be stable in ambient air for the duration of our 197 d experiment. Our computations predicted BiOI to be tolerant to vacancy and antisite defects, owing to high defect-formation energies and a high dielectric constant. In our photovoltaic devices, the BiOI thin film was sandwiched between  $NiO_x$  and ZnO charge transport layers. The EQEs,  $J_{SC}$  values, and power conversion efficiencies were improved over previous reports of BiOI devices, as well as other bismuth halides and bismuth chalcogenide materials. Our loss analyses showed that increasing carrier collection (e.g., by increasing the work function of the hole transport layer) and interface engineering (e.g., control of BiOI surface chemical state when depositing the electron transport layer) are key steps that can lead to future increases in efficiency. This work demonstrates that BiOI, previously considered to be a poor photocatalyst, has excellent potential as a lead-free, air-stable, defect-tolerant, and efficient photovoltaic material.

## Experimental Section

The full experimental methods are given in Section S1 (Supporting Information). The key details are given below.

**BiOI Synthesis:** BiOI thin films were grown by CVT inside a two-zone furnace. The furnace was preheated to 360 °C in zone 1 and 350 °C in zone 2. The substrates were loaded into the furnace in zone 2, but close to zone 1, and 300 mg BiI<sub>3</sub> (Alfa Aesar Puratronic, 99.999% purity on

**Table 4.** Bi/I ratio from fitting XPS core-level spectra.

BiOI thickness [nm]	220	440	720	720
ZnO overlayer	No	No	No	Yes
Bi/I ratio	1.0	1.0	1.0	1.7

a metals basis) loaded in a crucible was placed 2 cm away in zone 1. An Ar/O<sub>2</sub> gas mixture (19 mL min<sup>-1</sup> Ar and 4.5 mL min<sup>-1</sup> O<sub>2</sub>) was introduced to the closed tube. The growth times used and resulting BiOI film thicknesses are given in Section S3 (Supporting Information).

**Device Fabrication:** ITO/glass substrates (Colorado Concept Coatings LLC) were cleaned in acetone and isopropanol by sonication for 15 min each, followed by 10 min O<sub>2</sub> plasma treatment. NiO<sub>x</sub> was deposited on top by spin-casting a solution of 1 mol L<sup>-1</sup> nickel nitrate hexahydrate (Sigma-Aldrich) in ethylene glycol with 1 mol L<sup>-1</sup> ethylenediamine at 5000 rpm for 45 s. The films were annealed in air at 100 °C for 40 min, followed by 300 °C for 1 h. Following BiOI deposition on top, ZnO was deposited by AP-CVD. Diethylzinc (Sigma-Aldrich) was used as the Zn precursor, and 100 mL min<sup>-1</sup> oxygen gas (Air Products, <3 ppm H<sub>2</sub>O) as the oxidant. To complete the devices, 100 nm Al was thermally evaporated at <0.1–1 nm s<sup>-1</sup> through a shadow mask on top of ZnO under vacuum (5 × 10<sup>-6</sup> mbar). The device area was 4.5 mm<sup>2</sup>, as defined by the overlap between the Al top electrode and patterned ITO bottom electrode. For CH<sub>3</sub>NH<sub>3</sub>PbI<sub>3</sub> devices, PbI<sub>2</sub> (TCI) and CH<sub>3</sub>NH<sub>3</sub>I (Dyesol) were dissolved in 30 vol% dimethyl sulfoxide (Sigma-Aldrich) and 70 vol%  $\gamma$ -butyrolactone (Sigma-Aldrich) by mixing at 70 °C for 1 h. The solution was spun on the same NiO<sub>x</sub> on ITO used for BiOI devices at 1000 rpm for 30 s, followed by 4000 rpm for 60 s. 75  $\mu$ L toluene (Sigma-Aldrich) was dropped onto the spinning substrate 32 s from the end. The film was annealed at 60 °C for 2 min, followed by 100 °C for 30 min inside an N<sub>2</sub>-filled glovebox. 20 mg mL<sup>-1</sup> PC<sub>60</sub>BM (Solenne BV) in chlorobenzene (Sigma-Aldrich) was dynamically spun over the perovskite film at 1600 rpm for 40 s, followed by 3000 rpm for 10 s. The same Al electrodes were evaporated on top. A 3 mm<sup>2</sup> aperture was used to measure the CH<sub>3</sub>NH<sub>3</sub>PbI<sub>3</sub> devices to prevent edge effects.

**Characterization:** 2D X-ray diffraction patterns were collected using a Bruker General Area Detector Diffraction System (GADDS), and grazing incidence X-ray diffraction was performed with an incident angle of 0.5° using a Rigaku SmartLab instrument. Reflectance and transmittance measurements were made using a PerkinElmer Lambda 950 UV–vis–NIR spectrophotometer. The PL spectrum of BiOI was obtained using a Horiba LabRam Evolution multiline PL/Raman spectrometer with a confocal microscope. TCSPC measurements were performed with a 532 nm wavelength excitation laser using a single-photon-sensitive avalanche photodiode (Micro Photon Devices SPD-100-C0C). The XPS measurements in Figure 2 were performed on a Thermo Scientific K-Alpha spectrometer (photon energy of 1486.6 eV). In Figure 5, the XPS measurements were obtained using a monochromatic Al K <sub>$\alpha$</sub>  X-ray source ( $h\nu = 1486.6$  eV) with a SPECS PHOIBOS 150 electron energy analyzer. The composition of Bi and I were obtained by calculating the intensity ratio of the Bi 4f<sub>7/2</sub> and I 3d<sub>5/2</sub> peaks, taking into account the atomic sensitivity factors (4.25 for Bi 4f<sub>7/2</sub> and 4.6 for I 3d<sub>5/2</sub>). The UPS spectra were acquired in an Omicron ultrahigh-vacuum chamber with excitation provided by the He I emission line (21.22 eV) of a helium discharge lamp. Top-down scanning electron microscopy images in Figure 3 were obtained using an FEI Magellan (XHR 400L) scanning electron microscope. Solar simulations were performed using a Newport Oriol 92250A solar simulator and Keithley 2623A source-measure unit at 1 V s<sup>-1</sup>. EQE measurements were performed using a 250 W tungsten halogen lamp source with an Oriol Cornerstone 130 monochromator.

**Computational:** Calculations of the total energies of the host and defect supercells were performed using the *ab initio* total-energy and molecular dynamics program VASP (Vienna *ab initio* simulation program). Because of its quasi-2D layered nature, the structure of the pristine BiOI was fully relaxed (volume, cell-shape, and atomic position) using the optB86b-vdW van der Waals functional. Defect calculations were performed using a 4 × 4 × 4 Monkhorst–Pack *k*-point grid, with a plane-wave cutoff of 340 eV. The ionic and electronic dielectric constants were computed using density functional perturbation theory, as implemented in VASP. The subsequent atomic relaxations of the defect supercells were performed using the Perdew–Burke–Ernzerhof (PBE) functional form of the exchange–correlations functional, as described in detail in the Supporting Information. We note that we did not use GW and spin orbit coupling because this resulted in an overestimation of the bandgap.

## Supporting Information

Supporting Information is available from the Wiley Online Library or from the author, and includes the raw data for this work.

## Acknowledgements

The authors acknowledge Prof. Richard H. Friend, Prof. Mark W. B. Wilson, Dr. Charles Setters, Jeremy R. Poindexter, Dr. I. Marius Peters, Dr. Prashun Gorai and Charles Readman for useful discussions and technical assistance. R.L.Z.H. thanks Magdalene College, Cambridge. L.C.L. and J.L.M.-D. thank the EPSRC Centre for Doctoral Training: New and Sustainable Photovoltaics, and the Cambridge Winton Programme for the Physics of Sustainability for funding. T.N.H. thanks the Cambridge Graphene Centre, funded by the EPSRC. K.H.L.Z. was supported by the Herschel Smith fellowship. The U.S.-based theory and synthesis portions of this work were supported primarily as part of the Center for Next Generation Materials by Design (CNGMD), an Energy Frontier Research Center funded by the DOE Office of Science, Basic Energy Sciences under Contract No. DE-AC36-08GO28308. The MIT-based characterization portion of this work was supported primarily through a TOTAL SA research grant funded through MITe<sub>i</sub>, as well as a SusChem grant funded by the National Science Foundation (No. CBET-1605495). The TCSPC work was supported as part of the Center for Excitonics, an Energy Frontier Research Center funded by the U.S. Department of Energy, Office of Science, Office of Basic Energy Sciences under Award No. DE-SC0001088 (MIT). The computations were performed using resources sponsored by the Department of Energy's Office of Energy Efficiency and Renewable Energy and located at the NREL. The authors also acknowledge the MRSEC Shared Experimental Facilities at MIT, supported by the National Science Foundation (No. DMF-08019762). J.L.M.-D. conceived of the idea to investigate BiOI based on materials properties. R.L.Z.H., R.E.B., and T.B. simultaneously conceived of the idea to investigate BiOI based on the design criteria in ref. [5]. J.L.M.-D., L.C.L., and A.K. developed the CVT growth method. R.L.Z.H. performed bulk materials characterization, developed and characterized the devices, fitted the TCSPC measurements, performed the optical loss analysis, and fitted the XPS measurements. R.C.K. and V.S. performed the calculations. T.N.H. performed scanning electron microscopy and helped in device fabrication. K.H.L.Z. and R.E.B. performed XPS measurements. L.N. performed TCSPC measurements. M.S. performed UPS measurements. J.J. performed the photothermal deflection spectroscopy measurements and contributed to the footnote in ref. [19] on the abundance of bismuth. J.A.P. performed spectral PL measurements. All coauthors contributed to writing the manuscript.

## Conflict of Interest

The authors declare no conflict of interest.

## Keywords

air-stability, bismuth oxyiodide, defect-tolerance, *ns*<sup>2</sup> compounds, photovoltaics

Received: April 18, 2017

Revised: May 18, 2017

Published online:

[1] A. M. Ganose, C. N. Savory, D. O. Scanlon, *Chem. Commun.* **2017**, 53, 20.

[2] J. Seo, J. H. Noh, S. Il Seok, *Acc. Chem. Res.* **2016**, 49, 562.

- [3] W.-J. Yin, T. Shi, Y. Yan, *Appl. Phys. Lett.* **2014**, *104*, 63903.
- [4] S. D. Stranks, G. E. Eperon, G. Grancini, C. Menelaou, M. J. P. Alcocer, T. Leijtens, L. M. Herz, A. Petrozza, H. J. Snaith, *Science* **2013**, *342*, 341.
- [5] R. E. Brandt, V. Stevanović, D. S. Ginley, T. Buonassisi, *MRS Commun.* **2015**, *5*, 265.
- [6] A. Zakutayev, C. M. Caskey, A. N. Fioretti, D. S. Ginley, J. Vidal, V. Stevanović, E. Tea, S. Lany, *J. Phys. Chem. Lett.* **2014**, *5*, 1117.
- [7] A. J. Lehner, H. Wang, D. H. Fabini, C. D. Liman, C.-A. Hébert, E. E. Perry, M. Wang, G. C. Bazan, M. L. Chabiny, R. Seshadri, *Appl. Phys. Lett.* **2015**, *107*, 131109.
- [8] U. H. Hamdeh, R. D. Nelson, B. J. Ryan, U. Bhattacharjee, J. W. Petrich, M. G. Panthani, *Chem. Mater.* **2016**, *28*, 6567.
- [9] R. E. Brandt, R. C. Kurchin, R. L. Z. Hoye, J. R. Poindexter, M. W. B. Wilson, S. Sulekar, F. Lenahan, P. X. T. Yen, V. Stevanović, J. C. Nino, M. G. Bawendi, T. Buonassisi, *J. Phys. Chem. Lett.* **2015**, *6*, 4297.
- [10] B.-W. Park, B. Philippe, X. Zhang, H. Rensmo, G. Boschloo, E. M. J. Johansson, *Adv. Mater.* **2015**, *27*, 6806.
- [11] R. L. Z. Hoye, R. E. Brandt, A. Oshero, V. Stevanović, S. D. Stranks, M. W. B. Wilson, H. Kim, A. J. Akey, J. D. Perkins, R. C. Kurchin, J. R. Poindexter, E. N. Wang, M. G. Bawendi, V. Bulović, T. Buonassisi, *Chem. Eur. J.* **2016**, *22*, 2605.
- [12] S. Sun, S. Tominaka, J.-H. Lee, F. Xie, P. D. Bristowe, A. K. Cheetham, *APL Mater.* **2016**, *4*, 31101.
- [13] A. J. Lehner, D. H. Fabini, H. A. Evans, C.-A. Hébert, S. R. Smock, J. Hu, H. Wang, J. W. Zwanziger, M. L. Chabiny, R. Seshadri, *Chem. Mater.* **2015**, *9*, 7137.
- [14] M. B. Johansson, H. Zhu, E. M. J. Johansson, *J. Phys. Chem. Lett.* **2016**, *7*, 3467.
- [15] A. H. Slavney, T. Hu, A. M. Lindenberg, H. I. Karunadasa, *J. Am. Chem. Soc.* **2016**, *138*, 2138.
- [16] R. E. Brandt, J. R. Poindexter, R. C. Kurchin, P. Gorai, R. L. Z. Hoye, L. Nienhaus, M. W. B. Wilson, J. A. Polizzotti, R. Sereika, R. Žaltauskas, L. C. Lee, J. L. MacManus-Driscoll, M. G. Bawendi, V. Stevanović, T. Buonassisi, *Chem. Mater.* **2017**, *29*, 4667.
- [17] R. Jaramillo, M.-J. Sher, B. K. Ofori-Okai, V. Steinmann, C. Yang, K. Hartman, K. A. Nelson, A. M. Lindenberg, R. G. Gordon, T. Buonassisi, *J. Appl. Phys.* **2016**, *119*, 35101.
- [18] S. Sfaelou, D. Raptis, V. Dracopoulos, P. Lianos, *RSC Adv.* **2015**, *5*, 95813.
- [19] We note that the production of bismuth places a limit on the rate of deployment of BiOI and other bismuth-based solar absorbers. The availability of bismuth (10 200 tonnes year<sup>-1</sup> production; 370 000 tonnes global reserves) is lower than that of silicon or lead, but larger than that of tellurium (500 tonnes year<sup>-1</sup> production, 25 000 tonnes global reserves),<sup>[20,21]</sup> yet CdTe solar cells are already commercially available. Already with the 1.8% BiOI devices we report here using 900 nm thick BiOI, the cost to power production ratio for bismuth ( $2 \times 10^{-3} \$ W^{-1}$ ) is comparable to that of tellurium in CdTe solar cells ( $5 \times 10^{-3} \$ W^{-1}$ )<sup>[22]</sup> due to the lower cost of bismuth (\$10 kg<sup>-1</sup>) than tellurium (\$34 kg<sup>-1</sup>).<sup>[20]</sup> We therefore do not expect the commercial feasibility of BiOI photovoltaics to be limited by materials availability, global production, or price.
- [20] *Mineral Commodity Summaries*, U.S. Geological Survey, Reston, VA, USA **2017**.
- [21] M. Woodhouse, A. Goodrich, R. Margolis, T. James, R. Dhere, T. Gessert, T. Barnes, R. Eggert, D. Albin, *Sol. Energy Mater. Sol. Cells* **2012**, *115*, 199.
- [22] J. Jean, P. R. Brown, R. L. Jaffe, T. Buonassisi, V. Bulovic, *Energy Environ. Sci.* **2015**, *8*, 1200.
- [23] A. M. Ganose, M. Cuff, K. T. Butler, A. Walsh, D. O. Scanlon, *Chem. Mater.* **2016**, *28*, 1980.
- [24] K. Zhao, X. Zhang, L. Zhang, *Electrochem. Commun.* **2009**, *11*, 612.
- [25] K. Wang, F. Jia, Z. Zheng, L. Zhang, *Electrochem. Commun.* **2010**, *12*, 1764.
- [26] D. S. Bhachu, S. J. A. Moniz, S. Sathasivam, D. O. Scanlon, A. Walsh, S. M. Bawaked, M. Mokhtar, A. Y. Obaid, I. P. Parkin, J. Tang, C. J. Carmalt, *Chem. Sci.* **2016**, *7*, 4832.
- [27] B. Ahmmad, J. Kurawaki, T. Ohkubo, *J. Energy Eng.* **2013**, *139*, 338.
- [28] J. Barden, R. C. Powell, *Patent WO2013074345 A1*, **2013**.
- [29] R. L. Z. Hoye, P. Schulz, L. T. Schelhas, A. M. Holder, K. H. Stone, J. D. Perkins, D. Vigil-Fowler, S. Siol, D. O. Scanlon, A. Zakutayev, A. Walsh, I. C. Smith, B. C. Melot, R. C. Kurchin, Y. Wang, J. Shi, F. C. Marques, J. J. Berry, W. Tumas, S. Lany, V. Stevanović, M. F. Toney, T. Buonassisi, *Chem. Mater.* **2017**, *29*, 1964.
- [30] R. W. G. Wyckoff, *Cryst. Struct.* **1963**, *1*, 294.
- [31] C. Steffen, K. Thomas, U. Huniar, A. Hellweg, O. Rubner, A. Schroer, *J. Comput. Chem.* **2010**, *31*, 2967.
- [32] X. Zhang, C.-Y. Wang, L.-W. Wang, G.-X. Huang, W.-K. Wang, H.-Q. Yu, *Sci. Rep.* **2016**, *6*, 22800.
- [33] N. T. Hahn, S. Hoang, J. L. Self, C. B. Mullins, *ACS Nano* **2012**, *6*, 7712.
- [34] T. Todorov, O. Gunawan, S. Guha, *Mol. Syst. Des. Eng.* **2016**, *1*, 370.
- [35] S. Lany, A. Zunger, *Phys. Rev. B* **2008**, *78*, 235104.
- [36] H. Peng, D. O. Scanlon, V. Stevanovic, J. Vidal, G. W. Watson, S. Lany, *Phys. Rev. B* **2013**, *88*, 115201.
- [37] A. Goyal, P. Gorai, H. Peng, S. Lany, V. Stevanović, *Comput. Mater. Sci.* **2017**, *130*, 1.
- [38] V. Stevanović, S. Lany, X. Zhang, A. Zunger, *Phys. Rev. B* **2012**, *85*, 115104.
- [39] E. A. Kraut, R. W. Grant, J. R. Waldrop, S. P. Kowalczyk, *Phys. Rev. Lett.* **1980**, *44*, 1620.
- [40] E. M. Miller, D. M. Kroupa, J. Zhang, P. Schulz, A. R. Marshall, A. Kahn, S. Lany, J. M. Luther, M. C. Beard, C. L. Perkins, J. Van De Lagemaat, *ACS Nano* **2016**, *10*, 3302.
- [41] R. L. Z. Hoye, D. Muñoz-Rojas, K. P. Musselman, Y. Vaynzof, J. L. MacManus-Driscoll, *ACS Appl. Mater. Interfaces* **2015**, *7*, 10684.
- [42] N. T. Hahn, J. L. Self, C. B. Mullins, *J. Phys. Chem. Lett.* **2012**, *3*, 1571.
- [43] M. D. Irwin, D. B. Buchholz, A. W. Hains, R. P. H. Chang, T. J. Marks, *Proc. Natl. Acad. Sci. USA* **2008**, *105*, 2783.
- [44] S. Trasatti, *J. Electroanal. Chem. Interfacial Chem.* **1986**, *209*, 417.
- [45] R. L. Z. Hoye, B. Ehrler, M. L. Böhm, D. Muñoz-Rojas, R. M. Altamimi, A. Y. Alyamani, Y. Vaynzof, A. Sadhanala, G. Ercolano, N. C. Greenham, R. H. Friend, J. L. MacManus-Driscoll, K. P. Musselman, *Adv. Energy Mater.* **2014**, *4*, 1301544.
- [46] A. Polman, M. Knight, E. C. Garnett, B. Ehrler, W. C. Sinke, *Science* **2016**, *352*, 307.
- [47] R. E. Brandt, N. M. Mangan, J. V. Li, Y. S. Lee, T. Buonassisi, *J. Appl. Phys.* **2017**, *121*, 185301.
- [48] R. H. Kraichnan, *Proc. R. Soc. London* **1951**, *210*, 70.
- [49] H. Choi, C.-K. Mai, H.-B. Kim, J. Jeong, S. Song, G. C. Bazan, J. Y. Kim, A. J. Heeger, *Nat. Commun.* **2015**, *6*, 7348.
- [50] S. Bourdais, C. Choné, B. Delatouche, A. Jacob, G. Larramona, C. Moisan, A. Lafond, F. Donatini, G. Rey, S. Siebentritt, A. Walsh, G. Dennler, *Adv. Energy Mater.* **2016**, *6*, 1502276.
- [51] R. L. Z. Hoye, S. He, Y. Ievskaya, A. Sadhanala, A. Flewitt, R. H. Friend, J. L. MacManus-Driscoll, K. P. Musselman, *ACS Appl. Mater. Interfaces* **2014**, *6*, 22192.
- [52] T. Kirchartz, B. E. Pieters, J. Kirkpatrick, U. Rau, J. Nelson, *Phys. Rev. B* **2011**, *83*, 115209.